1 **EDDA 2.0: integrated simulation of debris flow initiation and dynamics, considering two initiation mechanisms**

4 Ping Shen[a], Limin Zhang[a] *, Hongxin Chen[b], Ruilin Fan[a]

6 * Corresponding author.

7 Email address: pshen@connect.ust.hk (P. Shen), cezhangl@ust.hk (L. M. Zhang),

8 chenhongxin@tongji.edu.cn (H. X. Chen), rfanaa@connect.ust.hk (R. L. Fan)

9 [a] Department of Civil and Environmental Engineering, The Hong Kong University of Science

10 and Technology, Clear Water Bay, Hong Kong

11 [b] Key Laboratory of Geotechnical and Underground Engineering of Ministry of Education,

12 Department of Geotechnical Engineering, Tongji University, China.

Abstract: Climate change results in more frequent rainstorms and more rain-induced debris flows in mountainous areas. The prediction of likely hazard zones is important for debris flow risk assessment and management. Existing numerical methods for debris flow analysis often require the input of hydrographs at prescribed initiation locations, ignoring the initiation process and leading to large uncertainties in debris flow initiation locations, times and volumes when applied to regional debris flow analysis. The evolution of the flowing mixture in time and space is hardly addressed either. This paper presents a new integrated numerical model, EDDA 2.0, to simulate the whole process of debris-flow initiation, motion, entrainment, deposition and property changes. Two physical initiation mechanisms are modeled: transformation from slope failures and surface erosion. Three numerical tests and field application to a catastrophic debris flow event are conducted to verify the model components and evaluate the model performance. The results indicate that the integrated model is capable of simulating the initiation and subsequent flowing process of rain-induced debris flows, as well as the physical evolution of the flowing mixture. The integrated model provides a powerful tool for analyzing multi-hazard processes, hazard interactions and regional debris-flow risk assessment in the future.

Keywords: debris flow; numerical modeling; rainfall infiltration; slope stability; erosion; entrainment.

1 Introduction

Debris flows are one of the most catastrophic hazards in mountainous areas (e.g. Zhang et al., 2013; Raia et al., 2014), and can pose high risks to society (e.g. Tang et al., 2011; Gao et al., 2016). They are often triggered by heavy rainfall and sensitive to climate change (e.g. Wong, 2009; Lee et al., 2010). As extreme rainstorms become more frequent, coping with rain-induced debris flows thus becomes critical in debris-flow prone regions such as Italy, Japan, Hong Kong and earthquake-affected areas in Sichuan, China.

During a storm, debris flows may be initiated by surface erosion, slope failures or dam breaching (e.g. Takahashi, 2007), and enlarged during the subsequent flowing process (e.g. Iverson, 1997). The debris flow mixture finally deposits in a flatter area, while the interstice fluid still flows along the debris flow track without further material entrainment as rainfall continues. The evolution of the flowing mixture includes three phases in terms of sediment concentration: clear water flow, hyperconcentrated flow and debris flow. The transition of the flowing mixture between any two phases occurs spatially and temporally during the whole process of rainfall.

Many numerical programs have been successfully developed for debris flow analysis, such as DAMBRK (Boss Corporation 1989), FLO-2D (O'Brien et al. 1993), DAN (Hungr 1995), DMM (Kwan and Sun 2006), Debris2D (Liu and Huang 2006), FLATModel (Medina et al. 2008), MassMov2D (Beguería et al. 2009), DAN3D (Hungr and McDougall 2009), PASTOR (Pastor et al. 2009), RAMMS (Bartelt et al., 2013), EDDA 1.0 (Chen and Zhang 2015), DebrisInterMixing (Boetticher et al., 2016) and AschFlow (Quan Luna et al., 2016). These programs can simulate the debris-flow movement with either constant or varying properties of the flowing mixture. The entrainment and deposition processes can also be considered, such as in EDDA 1.0 (Chen and Zhang, 2015).

Until now, numerical simulation of the physical process of debris flow initiation is

57   largely avoided in the literature. Moreover, very limited attempt has been made to simulate,

58   in an integrated manner, the entire process from the initiation to the subsequent debris-flow

59   motion and deposition. We address these two research gaps in this paper.

60   Experimental studies and field monitoring have been conducted to study the initiation

61   mechanics of rain-induced debris flows (e.g. Johnson and Sitar, 1990; Cui, 1992; Cannon et

62   al., 2001). A few physical models have been proposed (e.g. Takahashi, 1981; Iverson et al.,

63   1997) to reveal the mechanisms of initiation using infinite slope stability models which are

64   mathematically one-dimensional and statically determinate, leading to unambiguous

65   quantitative results. However, these models do not simulate the debris-flow initiation process,

66   particularly the transformation from a slope failure to a debris flow. Statistical models have

67   also been proposed to relate debris-flow initiation to rainfall (e.g. Caine, 1980; Wieczorek,

68   1987; Chen et al., 2005; Godt et al., 2006; Cannon et al., 2008; Coe et al., 2008; Guzzetti, et

69   al., 2008; Baum and Godt, 2010; Berti et al., 2012; Staley et al., 2013; Zhou and Tang, 2014;

70   De Luca and Versace, 2017a; De Luca and Versace, 2017b; Gao et al., 2017) and other

71   parameters such as surface runoff discharge (Berti and Simoni, 2005) or clay content (Chen et

72   al., 2010). These models are not physically-based.

73   Many of the existing computer programs do not simulate the initiation of debris flows.

74   Instead, they require a predefined empirical hydrograph, created based on the estimated

75   volumes of rainfall runoff and source materials, to initiate a debris flow, which is so called

76   "two-step" analysis (Fig. 1). The "two-step" analysis leads to large uncertainties in debris

77   flow initiation locations, times and volumes when applied to regional debris flow analysis.

78   For instance, Shen et al. (2017) simulated hillslope debris flows initiated from surface

79   erosion, in which the initiation location is artificially intervened (Fig. 1), and the slope failure

80   mechanisms is not included. The integrated simulation of the whole process of the debris

81   flow (Fig. 1) remains an open challenge. In addition, the physical rainfall runoff and overland

82   flow process before the initiation of debris flows is overlooked. Until now, the study on the

83   full evolution in time and space of the flowing mixture is limited.

84   Numerical tools have been developed for simulating a single type of hazards (e.g., Chen

85   et al., 2015; Shen et al., 2017). However, multiple types of hazards may be induced by a

86   rainstorm (i.e. slope failures, debris flows and flooding) (e.g. Zhang et al., 2014; Zhang et al.,

87   2017). One hazard can be the cause of another (e.g. rainfall triggers slope failures that in turn

88   trigger debris flows). Different types of hazards can also interact among each other (e.g.

89   several small debris flows from sub-channels can merger into a larger one). Hazard risk

90   assessment requires hydrological, landslide and debris flow analyses at a regional scale (e.g.

91   Formetta et al., 2011; Archfield et al., 2013). The simulation of the complete processes of

92   possible hazards and their interactions at a regional scale can be a powerful tool to help

93   identify likely hazards, their potentially affected areas and elements at risk. However, the

94   ability of numerical analysis of hazard interactions is still limited (e.g. Kappes et al., 2012;

95   Marzocchi et al., 2012). Using the existing "two-step" tools (Fig. 1) to analyze potential

96   regional hazards could be challenging, since it involves tremendous uncertainties and is

97   time-consuming to conduct the "two-step" analyses for each of all potential hazard locations

98   (e.g. Chen and Zhang, 2015; Gao et al., 2016; Shen et al, 2017). Hence the development of an

99   integrated model for simulating multi-hazard processes and interactions (Fig. 1) is of great

100   theoretical and practical importance.

101   The objectives of this paper are (1) to incorporate debris-flow initiation physically into

102   the debris-flow motion simulation to enable the simulation of the whole process of

103   rain-induced debris flows, (2) to study the full evolution of the flowing mixture in time and

104   space during the whole process of rainfall, and (3) to develop a tool to simulate multi-hazard

105   processes and analyze hazard interactions.

106

2 Methodology

2.1 Strategy of modeling initiation, dynamics and deposition of debris flows

Intense rainfall in mountainous regions could trigger debris flows from loose soil deposits on hill slopes or in channels. A conceptual model for rain-induced debris flows and likely initiation mechanisms are shown in Fig. 2. Debris flows can be initiated by three mechanisms: transformation from landslides, surface erosion and dam breaching. Due to rainfall infiltration, the hill slope gradually becomes saturated, and the soil loses its strength, causing shallow seated slope failures (Zhang et al., 2011). During a rainstorm, slope failures can occur at different times in space within a catchment. Some of the detached material may move into channels and form landslide dams, and some may transform into debris flows directly. As the surface runoff accumulates, the landslide dam formed earlier in the channel may break, initiating a channelized debris flow (e.g. Liu et al., 2009; Chen et al., 2012; Peng and Zhang, 2012). At the same time, the surface runoff may cause bed erosion and initiate hillslope debris flows (e.g. Cannon et al., 2001). Some of the separate debris flows may merge in the main channel of the drainage basin, forming a larger catastrophic debris flow event (e.g. Iverson et al., 1997). The final magnitude of a debris flow could be many times of its initial volume due to entrainment of materials along the path from additional slope failures, bed erosion or bank collapses (e.g. Iverson et al., 2011; Chen et al., 2012; Ouyang et al., 2015). If reaching a flat residential area downstream the basin, the developed debris flow can cause severe loss of lives and properties.

Based on the conceptual model for the whole process of debris flow in Fig. 2, the strategy of the integrated model, including two debris-flow initiation mechanisms (i.e. bed erosion and transformation from landslides) is shown in Fig. 3. The integrated model consists of a digital terrain module, a rainfall module, an infiltration module, an overland flow module, a slope stability module, a surface erosion module, a debris flow dynamics module

132 and a deposition module. The digital terrain module discretizes the study area into a grid

133 system with geological, hydrological and geotechnical information for each cell assigned. All

134 the computations are based on the concept of cell. As the primary triggering factor, rainfall is

135 simulated in the rainfall module. Then water infiltration into the ground is simulated to

136 analyze the pore water pressure profile and compute the surface runoff. The slope stability

137 and surface erosion are then evaluated in the slope stability module and surface erosion

138 module, respectively. Once debris flows are initiated by the two physical mechanisms, the

139 motion of the flowing mixture is analyzed through the debris flow dynamics module.

140 Material entrainment may occur along the flow path, incorporating solid materials from

141 addition slope failures and surface erosion. Finally, the deposition process is assessed through

142 the deposition module. The runout distance, inundation area and deposition volume of the

143 debris flows can all be assessed.

144

145 **2.2 Debris flow dynamics**

146 The core of the proposed integrated analysis is the debris-flow dynamics simulation and

147 constitutive modelling of the flowing mixture. The governing equations for debris flow

148 dynamics describe the mixture movement and changes in debris flow properties, which are

149 depth-integrated mass conservation equations (Equations 1 and 2) and momentum

150 conservation equations (Equations 3) (Chen and Zhang, 2015):

151
$$\frac{\partial h}{\partial t} + \frac{\partial (hv)}{\partial x} = i[C_{v*} + (1 - C_{v*})s_b] + A[C_{vA} + (1 - C_{vA})s_A] \tag{1}$$

152
$$\frac{\partial (C_v h)}{\partial t} + \frac{\partial (C_v hv)}{\partial x} + = iC_{v*} + AC_{vA} \tag{2}$$

153
$$\frac{\partial v}{\partial t} + v\frac{\partial v}{\partial x} = g\left[-\text{sgn}(v)S_f - \frac{\partial (z_b + h)}{\partial x}\right]$$
$$- \frac{v\{i[C_{v*} + (1 - C_{v*})s_b] + A[C_{vA} + (1 - C_{vA})s_A]\}}{h} \tag{3}$$

154   where h is the flow depth; v is the depth-integrated flow velocity (m/s); i is the erosion rate (>

155   0) or deposition rate (< 0) (m/s); A is the rate of material entrainment from detached landslide

156   materials (m/s); C_v is the volume fraction of solids in the flowing mixture; C_{v*} and C_{vA} are the

157   volume fraction in the erodible bed and in the entrained materials, respectively; s_b and s_A are

158   the degree of saturation of solids in the erodible bed and in the entrained materials,

159   respectively; S_f is the energy slope; z_b is the bed elevation (m); and the sgn (i.e. signum)

160   function is used to ensure that the direction of the flow resistance is opposite to that of the

161   flow direction.

162   One of the requirements of the integrated analysis is modeling different flowing mixtures

163   simultaneously. The flowing mixture can be classified into three types: clear water flow,

164   hyperconcentrated flow, and fully developed debris flow based on sediment concentration,

165   combining grain-size distribution and particle densities (Pierson, 2005). In this study, the

166   flowing types of mixtures are classified using the volumetric solid concentration C_v,

167   following FLO-2D Software Inc. (2009):

168   (1) If $C_v < 0.2$, the fluid mixture is deemed clear water flow which has a negligible yield

169   stress and a dynamic viscosity like that of water;

170   (2) If $0.2 < C_v < 0.45$, a hyperconcentrated flow develops with a certain level of

171   increased yield stress and dynamic viscosity;

172   (3) If $0.45 < C_v < 0.6$, the flowing mixture becomes a full debris flow with substantially

173   increased yield stress and dynamic viscosity.

174   Therefore, a proper rheological model must involve C_v to account for the changing

175   properties of the flowing mixture. We adopt different rheological models for different ranges

176   of C_v to deal with this problem. For clear water flow of which C_v is less than 0.2, the energy

177   slope S_f is based on Manning's equation. If $C_v > 0.2$, a quadratic rheological model developed

178   by O'Brien et al. (1993) is used:

179
$$S_f = \frac{\tau_y}{\rho gh} + \frac{K\mu V}{8\rho gh^2} + \frac{n_{td}^2 V^2}{h^{4/3}}$$
(4)

180 where ρ is the mass density of the flowing mixture (kg/m^3); τ_y, μ and n_{td} are the yield stress

181 (Pa), dynamic viscosity (Pa·s) and the equivalent Manning coefficient of the mixture,

182 respectively; K is the laminar flow resistance. n_{td} is expressed as (FLO-2D Software Inc.,

183 2009):

184
$$n_{td} = 0.0538ne^{6.0896C_v}$$
(5)

185 where n is the Manning coefficient. The following empirical relationships are adopted to

186 estimate τ_y and μ (O'Brien and Julien, 1988):

187
$$\tau_y = \alpha_1 e^{\beta_1 C_v}$$
(6)

188
$$\mu = \alpha_2 e^{\beta_2 C_v}$$
(7)

189 where α_1, α_2, β_1, and β_2 are empirical coefficients.

190

191 **2.3 Rainfall infiltration and convolution**

192   Under heavy rainfall, the excess xrainwater will become surface runoff when rainfall

193 intensity exceeds the infiltration capacity. In EDDA 2.0, the infiltration capacity is assumed

194 to be the saturated permeability of the surface soil. The surface runoff process is simulated by

195 solving the governing equations (Eqs. 1-3) and Manning's equation with i, A and C_v equal to

196 zero. The runoff water may cause surface erosion, or mix with landslide mass or flowing

197 mixture, which will be described later.

198   Water infiltration will increase the subsurface pore water pressure, causing slope failures

199 that are normally shallow-seated. The infiltration process is simulated in EDDA 2.0 by

200 solving the Richards equation with a forward-time central-difference numerical solution.

201 Non-uniform grid is created along the soil depth to enhance the accuracy of the solution near

202 boundaries and interfaces. The integrated program calculates the instant pore water pressure

203   profile to facilitate evaluating the slope stability of each cell at each time step.

204

205   **2.4 Initiation of debris flows from slope failures**

206   A debris flow may be initiated by transformation from a mass flow of slope failure

207   material at any location and at any time during a storm. The possible locations and

208   approximate failing time can be identified in a cell-based slope stability analysis, if the

209   topography, geology, soil properties etc. are defined properly. To consider this initiation

210   mechanism, the slope instability evaluation must be performed over all the computational

211   cells at each time step.

212   With the knowledge of real-time pore water pressure profiles provided by the infiltration

213   module, a real-time slope instability analysis can follow. Considering that these rain-induced

214   slope failures are shallow-seated, the thickness of the failure mass is small compared to the

215   large plan dimensions of these slopes. Therefore, an infinite slope model for two-layer soil

216   slopes is a reasonable option to evaluate the factor of safety (F_s) (Wu et al., 2016). Following

217   Chen and Zhang (2014), the search for the minimum F_s goes from the ground surface to the

218   wetting front where the volumetric water content changes significantly. If the minimum F_s is

219   smaller than 1, slope failure will occur at the depth corresponding to the minimum F_s. The

220   landslide mass is assumed to be a free-flowing mixture immediately after the slope failure,

221   with a pre-defined C_v value for the soil deposit and a flow depth the same as the failure depth.

222

223   **2.5 Initiation of debris flows due to bed erosion**

224   Intense rainfall can generate plentiful surface runoff, and the soil bed will erode in the

225   runoff water. The initially clear overland flow can gradually develop into a hyperconcentrated

226   flow and finally into a hillslope debris flow, as its C_v value increases through entrainment

227   from bed erosion. To consider this initiation mechanism, the erosion process is analyzed

228   within each computational cell at each time step.

229   We consider the occurrence of erosion under the condition that the bed shear stress is

230   equal or larger than the critical erosive shear stress of the bed material and the volumetric

231   sediment concentration is smaller than an equilibrium value. The equilibrium value proposed

232   by Takahashi et al. (1992) is adopted in this study:

233
$$C_{v\infty} = \frac{\rho_w \tan\theta}{(\rho_s - \rho_w)(\tan\phi_{bed} - \tan\theta)}$$
(8)

234   where ϕ_{bed} is the internal friction angle of the erodible bed; ρ_s is the density of soil particles

235   (kg/m^3); ρ_w is the density of water (kg/m^3); and θ is the slope angle.

236   Many researchers have studied the relationship between the soil erosion rate and shear

237   stress. A form of exponential expression has been used for bed erosion in the literature (e.g.

238   Roberts et al., 1998; Chen et al., 2015). More widely used is a linear function of shear stress

239   (e.g. Graf, 1984; Hanson and Simon, 2001; Julian and Torres, 2006; Chang et al., 2011; Chen

240   and Zhang, 2015):

241
$$i = K_e(\tau - \tau_c)$$
(9)

242   where i is the erosion rate (m/s); τ is the shear stress at the soil-water interface (Pa); K_e is the

243   coefficient of erodibility (m^3/N-s); τ_c is the critical erosive shear stress at the initiation of bed

244   erosion (Pa). The latter two parameters describe the erosion resistance of the bed soil and are

245   related to soil index properties (e.g. Chang et al., 2011; Zhu and Zhang, 2016). The shear

246   stress acting on the bed can be expressed as (e.g. Graf, 1984):

247
$$\tau = \rho g h S_f$$
(10)

248   where S_f is the energy slope.

249

250   **2.6 Material exchange: entrainment and deposition**

251   Material exchange occurs as debris flow marches along its flowing path, including

252   material entrainment (solid mass gain from outside of the flowing mixture) and deposition

253   (solid mass loss from inside of the flowing mixture).

254   The entrainment from additional bed erosion or slope failure materials along its

255   trajectory plays a significant role in debris flow volume amplification. The final volume of

256   the debris flow deposit could be many folds of its initial volume. An excellent example is the

257   1990 Tsing Shan debris flow that was the largest ever observed in Hong Kong. An originally

258   small slip of 350 m^3 developed into a final volume of 20,000 m^3 by entraining colluvium

259   along its flow path (King, 1996). In the integrated model, the landslide mass and surface

260   erosion are considered as the sources of material entrainment. The slope stability and surface

261   erosion evaluation module will be called for every computational cell at every time step;

262   hence the entrainment process is automatically considered once the two modules are called.

263   After flowing into a flatter area, deposition of some solid material will occur. Deposition

264   is deemed to occur if the flow velocity is smaller than a critical value and C_v is larger than the

265   equilibrium value described in Eq. 8. The deposition rate can be expressed as

266
$$i = \delta_d \left(1 - \frac{V}{pV_e} \right) \frac{C_{v\infty} - C_v}{C_{v*}} V \tag{11}$$

267   where V_e is the critical flow velocity following Takahashi et al. (1992); δ_d is a coefficient of

268   deposition rate; p (< 1) is a coefficient accounting for the location difference, and a value of

269   0.67 is recommended (Takahashi et al., 1992); V is the flow velocity; C_{v*} is the volume

270   fraction of solids in the erodible bed. The deposition condition is also detailed in Chen and

271   Zhang (2015).

272

273   **2.7 Numerical scheme**

274   The terrain is discretized into a grid of cells. Each cell is assigned with the input data,

275   including topography, soil depth, geotechnical soil properties, rheological model parameters

276 etc. There are eight flow directions in each cell: four compass directions and four diagonal

277 directions. In each time step, the infiltration is evaluated first to compute the surface runoff

278 and slope stability at each cell. Then changes in flow depth h and volumetric sediment

279 concentration C_v within each cell are evaluated considering the surface runoff, slope failure

280 mass entrainment, erosion, and deposition, followed by computing the flow velocity,

281 discharge and density along the eight flow directions of all the cells, with the averaged

282 surface roughness and slope between two cells computed. The changes in h and C_v due to the

283 flow exchange are evaluated finally at each cell.

284 After all the computations have been completed in each time step, numerical stability

285 criteria are checked for each cell to limit the time step to avoid surging while allowing for

286 large time steps. Three convergence criteria are adopted:

287 (1) The Courant-Friedrichs-Lewy (CFL) condition, with the physical interpretation that a

288   particle of fluid should not travel more than the cell size in one time step (Fletcher,

289   1990), is mostly used in explicit schemes. The time step is limited by

290            $$\Delta t \leq C \Delta x / (\beta V + c) \tag{12}$$

291   where C is the Courant number (C is not smaller than or equal to 1); m is a coefficient

292   (5/3 for a wide channel); c is the computed wave celerity.

293 (2) The percent change of flow depth in one time step should not exceed a specified

294   tolerant value, TOLP(h);

295 (3) The change in flow depth in one time step should not exceed a specified tolerant

296   value, TOL(h), which is applied when the flow moves to a cell with zero flow depth.

297 Adjusting these three criteria, the computational time and accuracy could reach a good

298 balance. If all the numerical stability criteria are successfully satisfied, the time step can be

299 increased for the next computational cycle. Otherwise the time step will be reduced and the

300 computation restarted. The volume conservation is computed at the end of each time step for

301   the inflow, outflow, grid system storage and infiltration loss.

302

303   **3   Model verification**

304   The previous version, EDDA 1.0 (Chen and Zhang, 2015), has passed several

305   verification tests including debris flow dynamics, erosion and deposition. In this new version

306   of integrated analysis, the new modules for surface runoff, coupled infiltration and slope

307   stability analysis, and the integrated program require further verification. The response of

308   Xiaojiagou Ravine during a rainstorm in August 2010 is used to verify the new modules. The

309   in-situ conditions shortly after the 2010 Xiaojiagou debris flow event are shown in Fig. 4.

310   The Xiaojiagou Ravine has an area of 7.84 km^2. The elevation of the ravine ranges between

311   1,100 m and 3,200 m. The hill slopes within the ravine are very steep with an average slope

312   angle of 46°. There are one main drainage channel and four branches within the Xiaojiagou

313   Ravine. The loose soil deposits on the hill slopes and channels of the ravine before the debris

314   flow event are identified based on field investigations and interpretation of satellite image

315   (e.g. Chen and Zhang, 2014). The rainstorm process triggering the catastrophic Xiaojiagou

316   debris flow is presented in Fig. 5. The rainstorm lasted about 40 hours with a total

317   precipitation of 220 mm. In this study, the rainfall is assumed to be uniformly distributed.

318   Spatial variational rainfall data can be used when a large area is considered, as the spatial

319   rainfall variation and the potential of triggering landslides are correlated (Gao et al, 2017).

320   First the performance of the rainfall-runoff module of the integrated program is

321   compared with a commonly used program FLO-2D (FLO-2D Software Inc., 2009). Then, the

322   infiltration module is checked against an analytical solution under steady rainfall. The slope

323   stability analysis is verified by comparing with the landslide satellite image and the

324   computation results by Chen and Zhang (2014). Finally, the performance of the integrated

325   model is checked against the 2010 Xiaojiagou debris flow event in Section 4.

326

3.1 Verification test 1: rainfall runoff

The same input data are used in EDDA 2.0 and FLO-2D, including the digital elevation model, Manning's coefficient ($n = 0.3$), the limiting Froude number ($L_f = 0.8$), the saturated permeability of the surface soil ($k_{st} = 3.6$ mm/h or 10^{-6} m/s) and the rainfall data (Fig. 5). Other hydrological parameters such as the soil porosities used in FlO-2D are adopted following Chen et al. (2013) and Shen et al. (2017).

The results from the two programs are compared in Fig. 6, including the distributions of the maximum flow depth and flow velocity. The result from FlO-2D (Figs. 6a and 6c) differ only slightly from those of EDDA 2.0 (Figs. 6b and 6d). During the rainstorm process, the maximum flow depth computed by FLO-2D is 3.2 m, while that by EDDA 2.0 is 3.4 m. The outflow hydrographs recorded at the mouth of the ravine of the two programs are shown in Fig. 7. The computed overall discharge processes from both programs are very close.

3.2 Verification test 2: infiltration process and resulting pore-water pressure changes

Before applying the infiltration module to compute the pore water pressure profiles under the actual rainfall event, four cases of infiltration under steady rainfall are adopted to verify the infiltration module. The results are compared with those from an analytical solution by Srivastava and Yeh (1991) and Zhan et al. (2013). The scenario of two-layer soil is considered, which is also used in the field application. Table 1 presents the input parameters for the four cases. Four combinations are set up to represent likely in-situ conditions. The results from the numerical infiltration module and the analytical solution are compared in Fig. 8. For all the four cases, the module performance is satisfactory.

351 **3.3 Verification test 3: slope stability analysis**

352   The 2008 Wenchuan earthquake triggered over 50,000 landslides within the earthquake

353 region, leaving a large amount of loose materials on hill slopes and in channels (Fig. 4).

354 These materials became the source of numerous post-earthquake rain-induced landslides and

355 debris flows. Until now, nearly 80% of such materials remained in the mountain regions,

356 posing great potential threats (Zhang et al., 2016). EDDA 2.0 is used to reproduce the slope

357 failures under the rainstorm in August 2010 (Fig. 5) by Chen and Zhang (2014), who

358 evaluated the slope stability of a 164.5 km^2 area near the epicenter. All the parameters are the

359 same as those in that study, with the only difference being that the area concerned in this

360 study is only Xiaojiagou Ravine (Fig. 4). The loose soil deposits are assumed to be two

361 layers. Given the same parameters such as the topography, layer thicknesses and soil

362 properties, the unstable cells when rainfall terminates are computed using the slope failure

363 module. Comparing the simulation results with the observation (Fig. 9), the computed

364 unstable cells generally fall upon the landslide scars formed during the rainstorm event.

365 Moreover, the results are compared with those by Chen and Zhang (2014), which have been

366 verified using the confusing matrix method (e.g. Van Den Eeckhaut et al., 2006). It is found

367 that the results of the two separate analyses are very similar. The computed total scar area is

368 4.42×10^5 m^2, comparing well with 5.20×10^5 m^2 from the satellite image. The difference is

369 15%. It is concluded that the proposed slope stability module performs reasonably well.

370

371 **4   Field application**

372 **4.1 Xiaojiagou debris flow on 14 August 2010**

373   A heavy rainstorm swept the epicenter, Yinxiu town, and its vicinity. The rainstorm

374 lasted about 40 h from 12 to 14 August 2010, pouring about 220 mm of precipitation in total

375 (Fig. 5). A catastrophic debris flow was triggered by the storm in Xiaojiagou Ravine (Fig. 4).

376   The debris flow was witnessed at the ravine mouth at about 5:00 am on 14 August and lasted

377   about 30 min. About 1.17×10^6 m^3 of the soil deposit was brought out of the Xiaojiagou

378   Ravine mouth in a form of a channelized debris flow. The runout material deposited in front

379   of the mouth, burying 1100 m of Province Road 303 (PR303), blocking Yuzixi River, forming

380   a debris flow barrier and raising the river bed by at least 15 m.

381

382   **4.2 Input information**

383   In EDDA 1.0, the study area has to be divided into two domains for rainfall runoff

384   simulation and debris-flow runout simulation respectively. However, in the integrated

385   simulation by EDDA 2.0, only one grid of 9500 cells 30×30 m in size is created (Fig. 2).

386   After the Xiaojiagou debris flow, detailed field investigations and laboratory tests were

387   conducted (Chen et al., 2012), as well as numerical back analysis (Chen et al., 2013). The

388   study area is divided into four zones by satellite interpretation: bare soil, vegetated soil, bed

389   rock and river bed (Chen and Zhang, 2014). The soil properties of each zone and the

390   constitutive (or rheological) parameters used in the integrated simulation are determined

391   following EDDA 1.0 (Chen and Zhang, 2015), shown in Tables 2-4. The erosion resistance

392   parameters τ_c and K_e of the soils are determined using the empirical equations based on field

393   tests in the Wenchuan earthquake zone (Chang et al., 2011):

394
$$\tau_c = 6.8 PI^{1.68} P^{-1.73} e^{-0.97} \tag{13}$$

395
$$K_e = 0.020075 e^{4.77} C_u^{-0.76} \tag{14}$$

396   where e is the void ratio; PI is the plasticity index; P is the fines content (< 0.063 mm); C_u is

397   the coefficient of uniformity. These four soil properties are determined to be 1.05, 18, 14 and

398   2000, respectively, according to Chang et al. (2011). Therefore, τ_c and K_e are estimated to be

399   8.7 Pa and 7.8×10^{-8} m^3/N-s, respectively. Uncertainties in the soil properties may also be

400   included when considering soil spatial variability (Xiao et al., 2017).

401

4.3 Integrated simulation results

We examine the final output of the integrated simulation first. Erosion plays an important role in the volume magnification of debris flows. The final erosion depths in the eroded areas are shown in Fig. 10a. The most eroded areas during the Xiaojiagou debris flow event were in channels, where a huge amount of loose solid material was present (Chen et al., 2012). Loose deposits on the hill slopes also eroded after the landslide bodies detached from their original locations and slid down the slopes. The distribution of the eroded areas reflects that the debris flows were initiated from both slope failures and surface erosion, then developed along the channels by further erosion and entrainment of the slope failure materials, which are the two mechanisms considered in the integrated model. The distribution of the maximum flow velocity is shown in Fig. 10b, with the maximum value being 9.5 m/s, which is very close to that from EDDA 1.0 (9.1 m/s). The slightly larger value of flow velocity from EDDA 2.0 is attributed to the consideration of the extra surface runoff within domain two created when using EDDA 1.0 (Fig. 2). The maximum velocity occurs in the ravine channels, indicating that the debris flow moves very rapidly.

The simulated and observed deposition areas are compared in Fig. 11. It is seen that the simulation results (Fig. 11a) match the observation (Fig. 11b) reasonably well. The simulated deposition depth is approximately 20 m, very close to that of the observed thickness of the deposit fan during the field investigations. The total volume of the observed deposition fan is about 1.17×10^6 m^3, while the simulated deposition volume of the debris flow is 0.9×10^6 m^3. The integrated model evaluates a smaller debris flow volume and the difference is about 23%. The main uncertainty arises from the slope failure module and surface erosion module.

The changes in the volumetric sediment concentration C_v and the discharge hydrograph at Section 1-1 (Fig. 4) are recorded during the simulation of the whole rainfall process, shown

426   in Fig. 12. The integrated model simulates two peaks in the discharge process throughout the

427   rainfall with a precursory boulder front arriving in advance. At around 12 h, the value of C_v

428   increases very quickly to a peak value of 0.6, indicating the arrival of the debris flow.

429   Afterwards, C_v decreases, which can be viewed as a hyperconcentrated flow or a clear water

430   flow after the debris flow passes. Another large debris flow surge is simulated at around 32 h

431   with the same pattern as the first one. The debris flow passes through Section 1-1 (Fig. 4)

432   first and continues to develop for some time. After most of the solid materials are brought

433   away by the debris flow surge, the flow at Section 1-1 becomes a hyperconcentrated flow,

434   and the flowing mixture gradually becomes a clear water flow as the rainwater continues to

435   generate surface runoff without further material entrainment. The integrated simulation is

436   capable of simulating multiple debris flow surges and the changes in the flowing mixture

437   properties throughout a rainfall event.

438   To demonstrate the evolution of the flowing mixture within the drainage basin, the

439   distributions of C_v at four snapshots during the storm are shown in Fig. 13. The recording

440   times of these four figures span a complete evolution cycle, i.e. clear water flow (Fig. 13a),

441   debris flow initiation (Fig. 13b), debris flow motion (Fig. 13c), and hyperconcentrated

442   flow/clear water flow (Fig. 13d). This evolution cycle could occur within the basin several

443   times in different branch channels, which can be captured by the integrated model.

444

445   **5   Limitations of EDDA 2.0**

446   We have successfully extended the "two-step" debris-flow simulation to an integrated

447   simulation of the whole process of rain-induced debris flows. However, there are still

448   limitations in the underlying assumptions and simplifications:

449   1. EDDA 2.0 considers the initiation of debris flows from transformation of slope

450   failures and surface erosion. However, the initiation from dam breaching has not yet

451   been tested.

452   2. The studies consider material entrainment from surface erosion and slope failure

453   detachment, but the entrainment from bank failures can only be considered using an

454   empirical rate, instead of through a three-dimensional physical model.

455   3. The governing equations are in a depth-integrated form; hence particle segregation

456   in the vertical direction cannot be considered.

457   4. The rheological models for the hyperconcentrated flow, fully developed debris flow

458   and slope failure mass flow need further study. Particularly, the slope failure mass

459   movement is critical for estimating the transformation rate from a slope failure to a

460   debris flow.

461

462 **6   Summary and conclusions**

463   A new integrated simulation model is developed for simulating rain-induced debris-flow

464 initiation, motion, entrainment, deposition and property changes. The model is unique in that

465 it simulates the whole process of rain-induced debris flow evolution and two physical

466 initiation mechanisms (i.e. transformation from landslides and surface erosion). Previous

467 "two-step analysis" with an assumed inflow hydrograph and an inflow location can now be

468 conducted at one go scientifically without subjective assumptions.

469   Three numerical tests have been conducted to verify the performance of the newly added

470 modules of the integrated model. The Xiaojiagou Ravine landslides and debris flows

471 triggered by the rainstorm in August 2010 were used as a verification case. In test 1, the

472 rainfall runoff simulation by EDDA 2.0 was compared to FLO-2D. The simulation results

473 from the two models are very close, which indicates that EDDA 2.0 simulates rainfall runoff

474 well. In test 2, an analytical solution for evaluating pore water pressure profile under

475 infiltration is adopted. Comparison between the model solution and the analytical solution

476   indicates that the integrated model evaluates the infiltration process well. The regional slope

477   stability within the study area under the same rainstorm was evaluated using the integrated

478   model in test 3. The computed unstable cells compare well with the observations from

479   satellite images and the results from previous studies.

480   The new integrated model was finally applied to reproduce the Xiaojiagou debris flow

481   event. The model can simulate the entire evolution process of rain-induced debris flows, and

482   estimates reasonably well the volume, inundated area and runout distance of the debris flow.

483   It is concluded that the new integrated debris flow simulation model, EDDA 2.0, is capable of

484   (1) simulating the whole process of rain-induced debris flow from debris-flow initiation to

485   post-initiation debris-flow motion, entrainment and deposition, and (2) tracing the evolution

486   of the flowing mixture in time and space during the whole process of rainfall. The integrated

487   model will serve as a powerful tool for analyzing multi-hazard processes and hazard

488   interactions, and assessment of regional debris-flow risks in the future.

489

490   *Code availability.* EDDA 2.0 is written in FORTRAN, which can be compiled using Intel

491   FORTRAN Compilers. A doi has been generated for the source code and the source code is

492   available online at http://doi.org/10.5281/zenodo.1033377. The source code is also available

493   online as a supplementary material to this paper. The main subroutine is "dfs.F90", which

494   presents the numerical solution algorithm for evaluating debris flow initiation from erosion

495   and slope failures, and for solving the governing equations of the dynamics of the flowing

496   mixture. An input file is needed ("edda_in.txt") for inputting material properties, hydrological

497   and rheological parameters and control settings. As an integrated program, EDDA 2.0 can be

498   used to analyse regional slope failures, so the "edda_in.txt" file also includes the material

499   properties and controlling options for slope stability analysis. Another input file

500   ("outflow.txt") is required to define the outflow cell. Digital terrain data (e.g. surface

501   elevation, slope gradient and erodible layer thickness) are included in separate ASCII grid

502   files and enclosed in the data folder. Output files are stored in the results folder and output

503   variables at selected points are stored in "EDDALog.txt".

504

505   ***Author contributions.*** Limin Zhang and Ping Shen conceived the methodology and

506   formulated the model. Ping Shen programmed the analysis code and performed the analysis.

507   Hongxin Chen and Ruilin Fan evaluated the model results. All authors contributed to the

508   writing of the manuscript.

509

510   ***Competing interests***. The authors declare that they have no conflict of interest.

511

512   ***Acknowledgements.*** The authors acknowledge the support from the Research Grants Council

513   of the Hong Kong SAR (No. C6012-15G and No. 16206217).

514

515   **References**

516   Archfield, S. A., Steeves, P. A., Guthrie, J. D., and Ries III, K. G.: Towards a publicly

517   available, map-based regional software tool to estimate unregulated daily streamflow at

518   ungauged rivers, Geosci. Model Dev., 6, 101-115, doi:10.5194/gmd-6-101-2013, 2013.

519   Baum, R. L. and Godt, J. W.: Early warning of rainfall-induced shallow landslides and debris

520   flows in the USA, Landslides, 7(3), 259-272, doi: 10.1007/s10346-009-0177-0, 2010.

521   Bartelt, P., Buehler, Y., Christen, M., Deubelbeiss, Y., Graf, C., McArdell, B., Salz, M., and

522   Schneider, M.: A numerical model for debris flow in research and practice, User Manual

523   v1.5 Debris Flow, WSL Institute for Snow and Avalanche Research SLF, Switzerland,

524   2013.

525   Beguería, S., Van Asch, Th. W. J., Malet, J.-P., and Gröndahl, S.: A GIS-based numerical

model for simulating the kinematics of mud and debris flows over complex terrain, Nat. Hazard Earth Sys., 9, 1897-1909, doi:10.5194/nhess-9-1897-2009, 2009.

Berti, M. and Simoni, A.: Experimental evidences and numerical modelling of debris flow initiated by channel runoff, Landslides, 2, 171-182, doi:10.1007/s10346-005-0062-4, 2005.

Berti, M., Martina, M. L. V., Franceschini, S., Pignone, S., Simoni, A., and Pizziolo, M.: Probabilistic rainfall thresholds for landslide occurrence using a Bayesian approach, J. Geophys. Res-Earth, 117(4), doi:10.1029/2012JF002367, 2012.

Boetticher, A. V., Turowski, J. M., McArdell, B. W., Rickenmann, D., and Kirchner, J. W.: DebrisInterMixing-2.3: a finite volume solver for three-dimensional debris-flow simulations with two calibration parameters - Part 1: Model description, Geosci. Model Dev., 9, 2909-2923, doi:10.5194/gmd-9-2909-2016, 2016.

Boss Corporation: DAMBRK-User's manual, Boss International Inc., Madison, Wisconsin, USA, 1989.

Caine, N.: The rainfall intensity: duration control of shallow landslides and debris flows, Geogr. Ann. A, 62, 23-27, doi: 10.2307/520449, 1980.

Cannon, S. H., Kirkham, R. M., and Parise, M.: Wildfire-related debris-flow initiation processes, Storm King Mountain, Colorado, Geomorphology, 39, 171-188, doi:10.1016/S0169-555X(00)00108-2, 2001.

Cannon, S. H., Gartner, J. E., Wilson, R., Bowers, J., and Laber, J.: Storm rainfall conditions for floods and debris flows from recently burned areas in southwestern Colorado and southern California, Geomorphology, 96(3-4), 250-269, doi: 10.1016/j.geomorph.2007.03.019, 2008.

Chang, D. S., Zhang, L. M., Xu, Y., and Huang, R. Q.: Field testing of erodibility of two landslide dams triggered by the 12 May Wenchuan earthquake, Landslides, 8, 321-332,

551   doi:10.1007/s10346-011-0256-x, 2011.

552 Chen, C. Y., Chen, T. C., Yu, F. C., Yu, W. H., and Tseng, C. C.: Rainfall duration and

553   debris-flow initiated studies for real-time monitoring, Environ. Geol., 47, 715-724,

554   doi:10.1007/s00254-004-1203-0, 2005.

555 Chen, H. X. and Zhang, L. M.: A physically-based distributed cell model for predicting

556   regional rainfall-induced shallow slope failures, Eng. Geol., 176, 79-92,

557   doi:10.1016/j.enggeo.2014.04.011, 2014.

558 Chen, H. X. and Zhang, L. M.: EDDA 1.0: integrated simulation of debris flow erosion,

559   deposition and property changes, Geosci. Model Dev., 8, 829-844,

560   doi:10.5194/gmd-8-829-2015, 2015.

561 Chen, H. X., Zhang, L. M., Chang, D. S., and Zhang, S.: Mechanisms and runout

562   characteristics of the rainfall-triggered debris flow in Xiaojiagou in Sichuan Province,

563   China, Nat. Hazards, 62, 1037-1057, doi:10.1007/s11069-012-0133-5, 2012.

564 Chen, H. X., Zhang, L. M., Zhang, S., Xiang, B., and Wang, X. F.: Hybrid simulation of the

565   initiation and runout characteristics of a catastrophic debris flow, J. Mt. Sci., 10,

566   219-232, doi:10.1007/s11629-013-2505-z, 2013.

567 Chen, H. X., Zhang, L. M., Gao, L., Zhu, H., and Zhang, S.: Presenting regional shallow

568   landslide movement on three-dimensional digital terrain, Eng. Geol., 195, 122-134,

569   doi:10.1016/j.enggeo.2015.05.027, 2015.

570 Chen, N. S., Zhou, W., Yang, C. L., Hu, G. S., Gao, Y. C., and Han, D.: The processes and

571   mechanism of failure and debris flow initiation for gravel soil with different clay

572   content, Geomorphology, 121, 222-230, doi:10.1016/j.geomorph.2010.04.017, 2010.

573 Chen, Z., Ma, L., Yu, S., Chen, S., Zhou, X., Sun, P., and Li, X.: Back analysis of the draining

574   process of the Tangjiashan barrier lake, J. Hydraul Eng., 141(4), 05014011, doi:

575   10.1061/(ASCE)HY.1943-7900.0000965, 2015.

576   Coe, J. A., Kinner, D. A., and Godt, J. W.: Initiation conditions for debris flows generated by

577   runoff at Chalk Cliffs, central Colorado, Geomorphology, 96, 270-297,

578   doi:10.1016/j.geomorph.2007.03.017, 2008.

579   Cui, P.: Study on condition and mechanisms of debris flow initiation by means of experiment,

580   Chinese Sci. Bull., 37, 759-763, 1992.

581   De Luca D. L. and Versace P. A.: Comprehensive framework for empirical modeling of

582   landslides induced by rainfall: the Generalized FLaIR Model (GFM), Landslides, 14(3),

583   1009-1030, ISSN: 1612-5118, DOI: 10.1007/s10346-016-0768-5, 2017a.

584   De Luca, D. L. and Versace, P.: Diversity of Rainfall Thresholds for early warning of

585   hydro-geological   disasters,   Adv.   Geosci.,   44,   53-60,

586   https://doi.org/10.5194/adgeo-44-53-2017, 2017b.

587   Fletcher, C. A. J.: Computational Techniques for Fluid Dynamics, Volume I, 2nd ed.,

588   Springer-Velag, New York, 1990.

589   FLO-2D Software Inc.: FLO-2D reference manual, Nutrioso, Arizona, USA, 2009.

590   Formetta, G., Mantilla, R., Franceschi, S., Antonello, A., and Rigon, R.: The JGrass-NewAge

591   system for forecasting and managing the hydrological budgets at the basin scale: models

592   of flow generation and propagation/routing, Geosci. Model Dev., 4, 943-955,

593   doi:10.5194/gmd-4-943-2011, 2011.

594   Gao, L., Zhang, L. M., Chen, H. X., and Shen, P.: Simulating debris flow mobility in urban

595   settings, Eng. Geol., 214, 67-78, doi:10.1016/j.enggeo.2016.10.001, 2016.

596   Gao, L., Zhang, L. M., and Cheung, R. W. M.: Relationships between natural terrain landslide

597   magnitudes and triggering rainfall based on a large landslide inventory in Hong Kong,

598   Landslides, 15(4), 727-740, doi: 10.1007/s10346-017-0904-x, 2017.

599   Gao, L., Zhang, L. M., and Lu, M. Q.: Characterizing the spatial variations and correlations

600   of large rainstorms for landslide study. Hydrol. Earth Sys. Sci., 21(9), 4573-4589, doi:

601   10.5194/hess-21-4573-2017, 2017.

602   Godt, J. W., Baum, R. L., and Chleborad, A. F.: Rainfall characteristics for shallow

603   landsliding in Seattle, Washington, USA. Earth Surf. Proc. Land, 31, 97-110, doi:

604   10.1002/esp.1237, 2006.

605   Graf, W. H.: Hydraulics of sediment transport, Water Resources Publications, Colorado,

606   1984.

607   Guzzetti, F., Peruccacci, S., Rossi, M., and Stark, C. P.: The rainfall intensity-duration control

608   of shallow landslides and debris flows: An update, Landslides, 5, 3-17, doi:

609   10.1007/s10346-007-0112-1, 2008.

610   Hanson, G. J. and Simon, A.: Erodibility of cohesive streambeds in the loess area of the

611   midwestern USA, Hydrolo. Process., 15(1), 23-38, doi: 10.1002/hyp.149, 2001.

612   Hungr, O.: A model for the runout analysis of rapid flow slides, debris flows, and avalanches,

613   Can. Geotech. J., 32, 610-623, doi:10.1139/t95-063, 1995.

614   Hungr, O. and McDougall, S.: Two numerical models for landslide dynamic analysis,

615   Computat. Geosci., 35(5), 978-992, doi: 10.1016/j.cageo.2007.12.003, 2009.

616   Iverson, R. M.: The physics of debris flows, Rev. Geophys., 35(3), 245-296, doi:

617   10.1029/97RG00426, 1997.

618   Iverson, R. M., Reid, M. E., and LaHusen, R. G.: Debris-flow mobilization from landslides,

619   Annu. Rev. Earth Pl. Sc., 25(1), 85-138, doi: 10.1146/annurev.earth.25.1.85, 1997.

620   Iverson, R. M., Reid, M. E., Logan, M., LaHusen, R. G., Godt, J. W., and Griswold, J. P.:

621   Positive feedback and momentum growth during debris-flow entrainment of wet bed

622   sediment, Nat. Geosci., 4, 116-121, doi:10.1038/ngeo1040, 2011.

623   Johnson, K. A. and Sitar, N.: Hydrologic conditions leading to debris-flow initiation, Can.

624   Geotech. J., 27, 789-801, doi:10.1139/t90-092, 1990.

625   Julian, J. P. and Torres, R.: Hydraulic erosion of cohesive riverbanks, Geomorphology,

76(1-2), 193-206, doi: 10.1016/j.geomorph.2005.11.003, 2006.

Kappes, M. S., Keiler, M., von Elverfeldt, K. and Glade, T.: Challenges of analyzing multi-hazard risk: a review, Nat. Hazards, 64(2), 1925-1958, doi: 10.1007/s11069-012-0294-2, 2012.

King, J.: Tsing Shan debris flow, Special Project Report SPR 6/96, Geotechnical Engineering Office, Hong Kong Government, 133, 1996.

Kwan, J. S. and Sun, H.: An improved landslide mobility model, Can. Geotech. J., 43(5), 531-539, doi: 10.1139/t06-010, 2006.

Lee, B. Y., Mok, H. Y., and Lee, T. C.: The latest on climate change in Hong Kong and its implications for the engineering sector, DHKO in the HKIE Conf. on Climate Change - Hong Kong Engineers' Perspective, Hong Kong Observatory, Government of Hong Kong SAR, Hong Kong, 2010.

Liu, K. F. and Huang, M. C.: Numerical simulation of debris flow with application on hazard area mapping, Computat. Geosci., 10, 221-240, doi: 10.1007/s10596-005-9020-4, 2006.

Liu, N., Zhang, J. X., Lin, W., Cheng, W. Y., and Chen, Z. Y.: Draining Tangjiashan Barrier Lake after Wenchuan Earthquake and the flood propagation after the dam break, Sci. China Ser. E., 52(4), 801–809, doi: 10.1007/s11431-009-0118-0, 2009.

Marzocchi, W., Garcia-Aristizabal, A., Gasparini, P., Mastellone, M. L., and Di Ruocco, A.: Basic principles of multi-risk assessment: a case study in Italy, Nat. Hazards, 62(2), 551-573, doi: 10.1007/s11069-012-0092-x, 2012.

Medina, V., Hürlimann, M., and Bateman, A.: Application of FLATModel, a 2-D finite volume code, to debris flows in the northeastern part of the Iberian Peninsula, Landslides, 5, 127-142, doi: 10.1007/s10346-007-0102-3, 2008.

O'Brien, J. S. and Julien, P. Y.: Laboratory analysis of mudflow properties, J. Hydraul. Eng., 114, 877-887, doi: 10.1061/(ASCE)0733-9429(1988)114:8(877), 1988.

651 O'Brien, J. S., Julien, P. Y., Fullerton, W. T.: Two-dimensional water flood and mudflow

652 simulation, J. Hydraul. Eng., 119, 244-261, doi:

653 10.1061/(ASCE)0733-9429(1993)119:2(244), 1993.

654 Ouyang, C., He, S., and Tang, C.: Numerical analysis of dynamics of debris flow over

655 erodible beds in Wenchuan earthquake-induced area, Eng. Geol., 194, 62-72, doi:

656 10.1016/j.enggeo.2014.07.012, 2015.

657 Pastor, M., Haddad, B., Sorbino, G., Cuomo, S., and Drempetic, V.: A depth-integrated,

658 coupled SPH model for flow-like landslides and related phenomena, Int. J. Numer. Anal.

659 Met., 33(2), 143-172, doi: 10.1002/nag.705, 2009.

660 Peng, M., and Zhang, L.M.: Breaching parameters of landslide dams, Landslides, 9(1): 13–

661 31, doi: 10.1007/s10346-011-0271-y, 2012.

662 Pierson, T. C.: Hyperconcentrated flow - transitional process between water flow and debris

663 flow. In Debris-flow hazards and related phenomena (eds. Jakob, M. and Hungr, O.),

664 Springer-Praxis, Chichester, UK, 159-202, doi: 10.1007/3-540-27129-5_8, 2005.

665 Quan Luna, B., Blahut, J., van Asch, T., van Westen, C., and Kappes, M.: ASCHFLOW-A

666 dynamic landslide run-out model for medium scale hazard analysis, Geoenvironmental

667 Disasters, 3(1), 29, 10.1186/s40677-016-0064-7, 2016.

668 Raia, S., Alvioli, M., Rossi, M., Baum, R. L., Godt, J. W., and Guzzetti, F.: Improving

669 predictive power of physically based rainfall-induced shallow landslide models: a

670 probabilistic approach, Geosci. Model Dev., 7, 495-514, doi:10.5194/gmd-7-495-2014,

671 2014.

672 Roberts, J., Jepsen, R., Gotthard, D., and Lick, W.: Effects of particle size and bulk density on

673 erosion of quartz particles, J. Hydraul Eng., doi:

674 10.1061/(ASCE)0733-9429(1998)124:12(1261), 1261-1267, 1998.

675 Shen, P., Zhang, L. M., Chen, H. X., and Gao, L.: Role of vegetation restoration in mitigating

676   hillslope   erosion   and   debris   flows,   Eng.   Geol.,   216,   122-133,   doi:

677   10.1016/j.enggeo.2016.11.019, 2017.

678 Srivastava, R. and Yeh, T. C. J.: Analytical solutions for one-dimensional, transient

679   infiltration toward the water table in homogeneous and layered soils, Water Resour.

680   Res., 27, 753-762, doi:10.1029/90WR02772, 1991.

681 Staley, D. M., Kean, J. W., Cannon, S. H., Schmidt, K. M., and Laber, J. L.: Objective

682   definition of rainfall intensity–duration thresholds for the initiation of post-fire debris

683   flows   in   southern   California,   Landslides,   10(5),   547-562,   doi:

684   10.1007/s10346-012-0341-9, 2013.

685 Takahashi, T.: Debris flow, Annu. Rev. Fluid Mech., 13, 57-77, 1981.

686 Takahashi, T.: Debris flow: mechanics, prediction and countermeasures, Taylor & Francis,

687   London, UK, 2007.

688 Takahashi, T., Nakagawa, H., Harada, T., and Yamashiki, Y.: Routing debris flows with

689   particle   segregation,   J.   Hydraul.   Eng.,   118,   1490-1507,

690   doi:10.1061/(ASCE)0733-9429(1992)118:11(1490), 1992.

691 Tang, C., Rengers, N., van Asch, Th.W.J., Yang, Y. H., and Wang, G. F.: Triggering conditions

692   and depositional characteristics of a disastrous debris flow event in Zhouqu city, Gansu

693   Province,   northwestern   China,   Nat.   Hazard   Earth   Sys.,   11,   2903-2912,

694   doi:10.5194/nhess-11-2903-2011, 2011.

695 Van Den Eeckhaut, M., Vanwalleghem, T., Poesen, J., Govers, G., Verstraeten, G.,

696   Vandekerckhove, L.: Prediction of landslide susceptibility using rare events logistic

697   regression: a case-study in the Flemish Ardennes (Belgium), Geomorphology, 76(3),

698   392-410, doi: 10.1016/j.geomorph.2005.12.003, 2006.

699 Wieczorek, G. F.: Effect of rainfall intensity and duration on debris flows in central Santa

700   Cruz Mountains, California, Rev. Eng. Geol., 7, 93-104, doi:10.1130/REG7-p93, 1987.

701 Wong, H. N.: Rising to the challenges of natural terrain landslides, Natural Hillsides: Study

702 and Risk Management Measures, Proc., 29th Annual Seminar of the HKIE Geotechnical

703 Division, Hong Kong Institution of Engineers, Hong Kong, 15-53, 2009.

704 Wu, L. Z., Selvadurai, A. P. S., Zhang, L. M., Huang, R. Q., and Huang, J.: Poro-mechanical

705 coupling influences on potential for rainfall-induced shallow landslides in unsaturated

706 soils, Adv. Water Resour., 98, 114-121, doi: 10.1016/j.advwatres.2016.10.020, 2016.

707 Xiao, T., Li, D. Q., Cao, Z. J., and Tang, X. S.: Full probabilistic design of slopes in spatially

708 variable soils using simplified reliability analysis method, Georisk, 11(1), 146-159, doi:

709 10.1080/17499518.2016.1250279, 2017.

710 Zhan, T. L., Jia, G. W., Chen, Y. M., Fredlund, D. G., and Li, H.: An analytical solution for

711 rainfall infiltration into an unsaturated infinite slope and its application to slope stability

712 analysis, Int. J. Numer. Anal. Met., 37, 1737-1760, doi:10.1002/nag.2106, 2013.

713 Zhang, L. L., Zhang, J., Zhang, L. M., and Tang, W. H.: Stability analysis of rainfall-induced

714 slope failure: a review, Proceedings of the ICE-Geotechnical Engineering, 164, 299,

715 2011.

716 Zhang, L. M., Zhang, S., and Huang, R. Q.: Multi-hazard scenarios and consequences in

717 Beichuan, China: The first five years after the 2008 Wenchuan earthquake, Engineering

718 Geology, 180, 4-20, 2014.

719 Zhang, S., and Zhang, L.M.: Impact of the 2008 Wenchuan earthquake in China on

720 subsequent long-term debris flow activities in the epicentral area, Geomorphology,

721 276(1), 86-103, doi: 10.1016/j.geomorph.2016.10.009, 2017.

722 Zhang, S., Zhang, L. M., Chen, H. X., Yuan, Q., and Pan, H.: Changes in runout distances of

723 debris flows over time in the Wenchuan Earthquake zone, J. Mt. Sci., 10, 281-292,

724 doi:10.1007/s11629-012-2506-y, 2013.

725 Zhang, S., Zhang, L. M., Lacasse, S., and Nadim, F.: Evolution of mass movements near

726   epicentre of Wenchuan earthquake, the first eight years. Sci. Rep., 6, 36154, 2016.

727   Zhou, W. and Tang, C.: Rainfall thresholds for debris flow initiation in the Wenchuan

728   earthquake-stricken area, southwestern China, Landslides, 11, 877-887,

729   doi:10.1007/s10346-013-0421-5, 2014.

730   Zhu, H., and Zhang, L.M.: Field investigation of erosion resistance of common grass species

731   for soil-bioengineering in Hong Kong, Acta Geotechnica, 11(5), 1047–1059, doi:

732   10.1007/s11440-015-0408-6, 2016.

733   **List of Captions**

734

735   *Table captions*

736   **Table 1.** Parameters used in the infiltration module verification.

737   **Table 2.** Properties of four types of superficial materials.

738   **Table 3.** Soil properties for debris flow simulation.

739   **Table 4.** Constitutive (rheological) parameters for debris flow simulation.

740

741   *Figure captions*

742   **Figure 1.** Conceptual model of a rain-induced debris flow and three typical initiation
743   mechanisms of debris flows: bed erosion, transformation from landslide, and dam
744   breach.

745   **Figure 2.** Comparison between "two-step" simulation and integrated simulation of
746   rain-induced debris flows.

747   **Figure 3.** Framework of the integrated simulation of debris flows.

748   **Figure 4.** A satellite image of the study area taken shortly after the Xiaojiagou debris flow on
749   14 August 2010.

750   **Figure 5.** Rainfall process of the August 2010 rainstorm.

751   **Figure 6.** Comparison of the maximum surface runoff flow depths and flow velocities
752   simulated using FLO-2D [(a) and (b)] and EDDA 2.0 [(c) and (d)].

753   **Figure 7.** Comparison of the outflow hydrographs at the ravine mouth using FLO-2D and
754   EDDA 2.0.

755   **Figure 8.** Pore water pressure profiles at various times: (a) Case 1; (b) Case 2; (c) Case 3; (d)
756   Case 4.

757   **Figure 9.** Computed unstable cells vs. landslide scars on the satellite image.

758   **Figure 10.** Simulation results of the Xiaojiagou debris flow: (a) final shape and depth of the
759   erosion zone; (b) maximum flow velocity.

760   **Figure 11.** Comparison of the simulated and observed deposition zones: (a) simulation result;
761   (b) enlarged view of the observed deposition area (Chen and Zhang, 2015).

762   **Figure 12.** Outflow hydrograph and changes in C_v at the Xiaojiagou Ravine mouth during the
763   simulation period.

764   **Figure 13.** Distribution of C_v at different times of the storm event: (a) clear water flow; (b)
765   initiation of debris flow; (c) channelized debris flow; (d) post hyperconcentrated/clear
766   water flow.

Table 1. Parameters used in the infiltration module verification.

Case	Vertical depth (cm)	α (cm^{-1})	θ_s	θ_r	k_s (cm/h)	q_a	q_b	γ (°)	Rainfall duration (h)
1	100	0.1	0.40	0.06	10	0.1	0.9	0	20
	100				1				
2	100	0.01	0.40	0.06	1	0.1	0.9	0	20
	100				10				
3	400	0.01	0.42	0.18	3.6	0	$0.4k_{st}$	40	20
	100		0.30	0.10	0.036				
4	400	0.01	0.42	0.18	3.6	0	k_{st}	40	20
	100		0.30	0.10	0.036				

Notes: α = constitutive parameter; θ_s = saturated water content; θ_r = residual water content; k_s = saturated permeability; q_a = antecedent rainfall intensity; q_b = rainfall intensity for time greater than zero; γ = slope angle. Parameters α, θ_s and θ_r are used in the constitutive relations between the hydraulic conductivity and moisture content and the pressure head (Srivastava and Yeh, 1991).

Table 2. Properties of four types of superficial materials.

Geological type	c' (kPa)	ϕ' (°)	γ_{sat} (kN/m^3)	K_s (m/s)	α (cm^{-1})	θ_s	θ_r
Vegetated land	10.5	37	21	1×10^{-6}	0.8	0.40	0.25
Bed rock	-	-	-	0	-	-	-
Loose soil deposit	4	37	21	1×10^{-5}	0.8	0.42	0.18
Riverbed	-	-	-	1×10^{-3}	-	-	-

Notes: c' = true cohesion of soil; ϕ' = friction angle of soil; γ_{sat} = unit weight of solid particles; K_s = saturated permeability of soil.

Table 3. Soil properties for debris flow simulation.

d_{50} (mm)	ρ_s (kg/m^3)	C_{v*}	s_b	τ_c (Pa)	K_e (m^3/N-s)
35	2650	0.65	1	8.7	78.5×10^{-9}

Notes: d_{50} = mean grain size; ρ_s = density of solid particles; C_{v*} = volume fraction of solids in the erodible bed; s_b = degree of saturation of the erodible bed; τ_c = critical erosive shear stress; K_e = coefficient of erodibility.

Table 4. Constitutive (rheological) parameters for debris flow simulation.

α_1 (kPa)	β_1	α_2 (Pa·s)	β_2	K	δ_d	n
3.8	3.51	0.02	2.97	2500	0.02	0.16

Notes: α_1, β_1 = empirical coefficients for calculating τ_y; α_2, β_2 = empirical coefficients for calculating μ; K = laminar flow resistance coefficient; δ_d = deposition coefficient; n = Manning's coefficient.
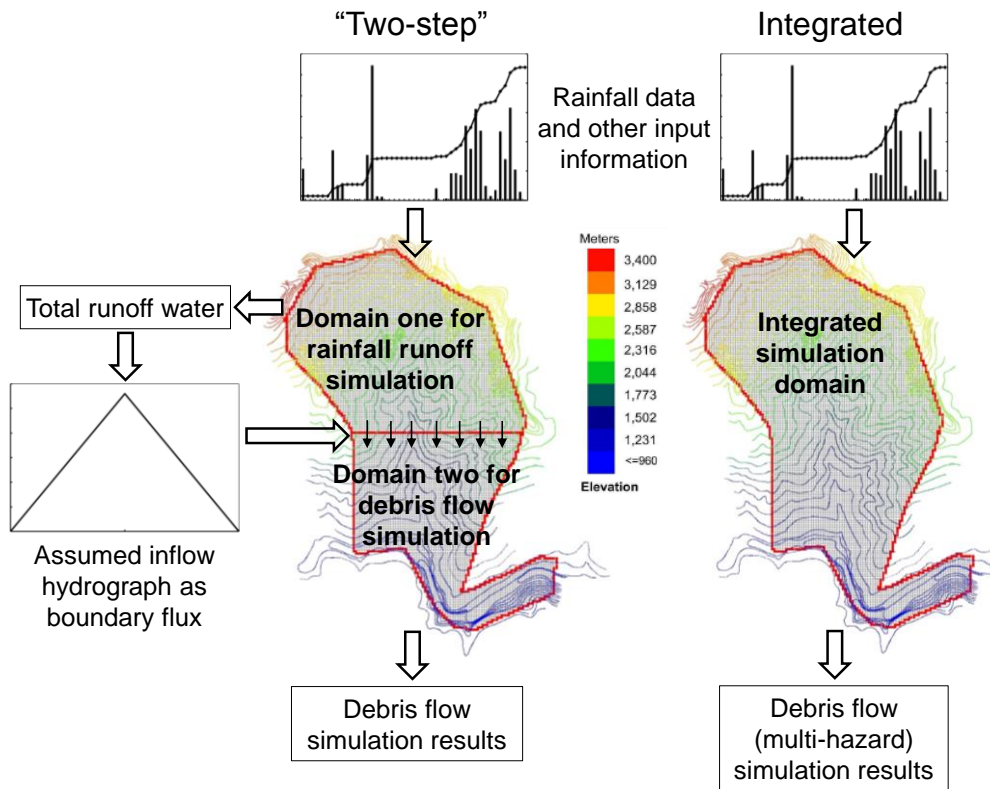
Figure 1. Comparison between "two-step" simulation and integrated simulation of rain-induced debris flows.
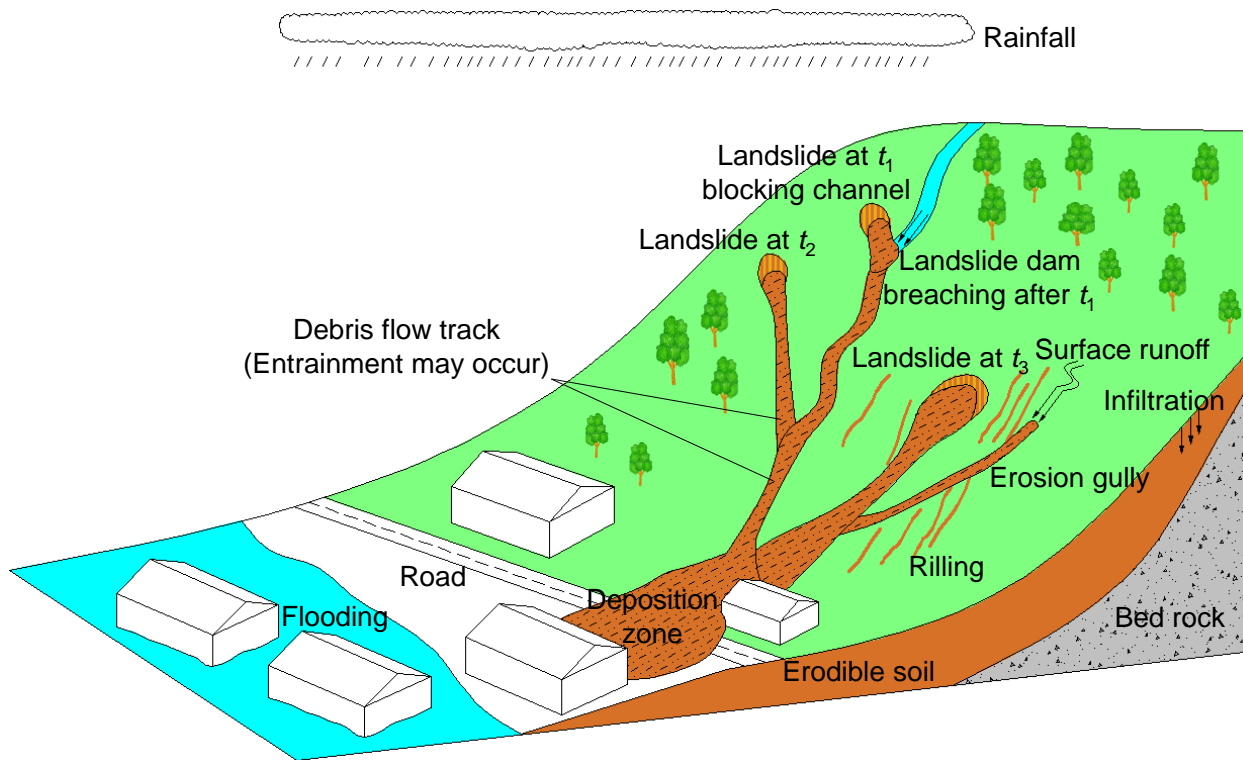
Figure 2. Conceptual model of a rain-induced debris flow and three typical initiation mechanisms of debris flows: bed erosion, transformation from landslide, and dam breach.
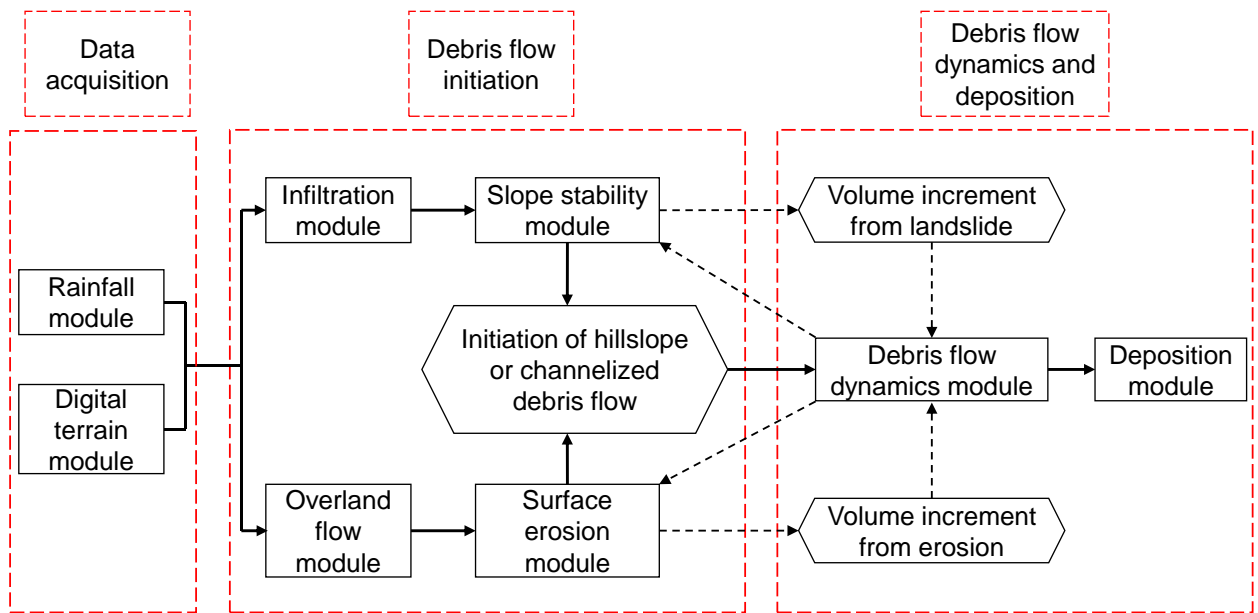
Figure 3. Framework of the integrated simulation of debris flows.
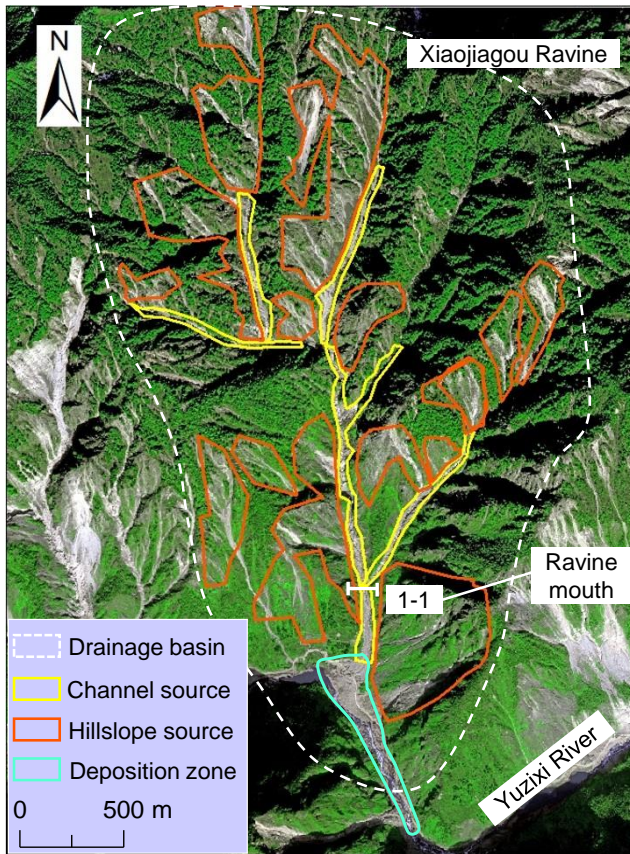
Figure 4. A satellite image of the study area taken shortly after the Xiaojiagou debris flow on 14 August 2010.
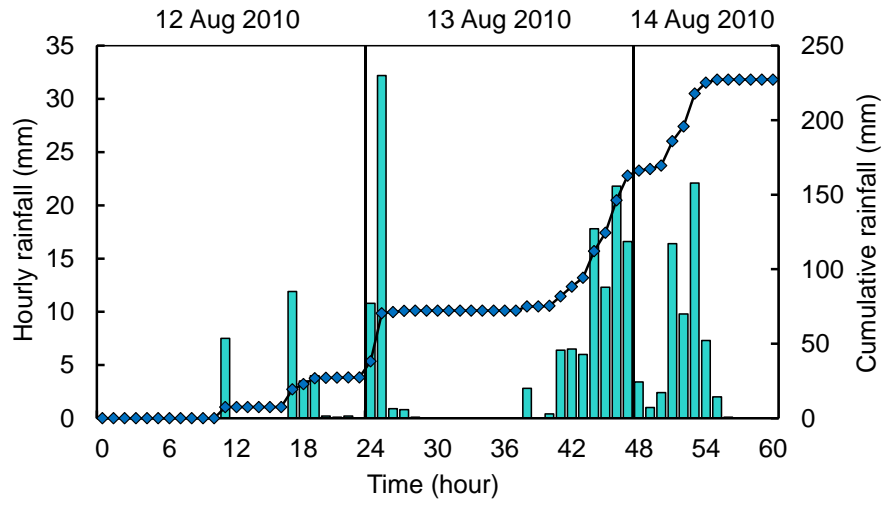
Figure 5. Rainfall process of the August 2010 rainstorm.
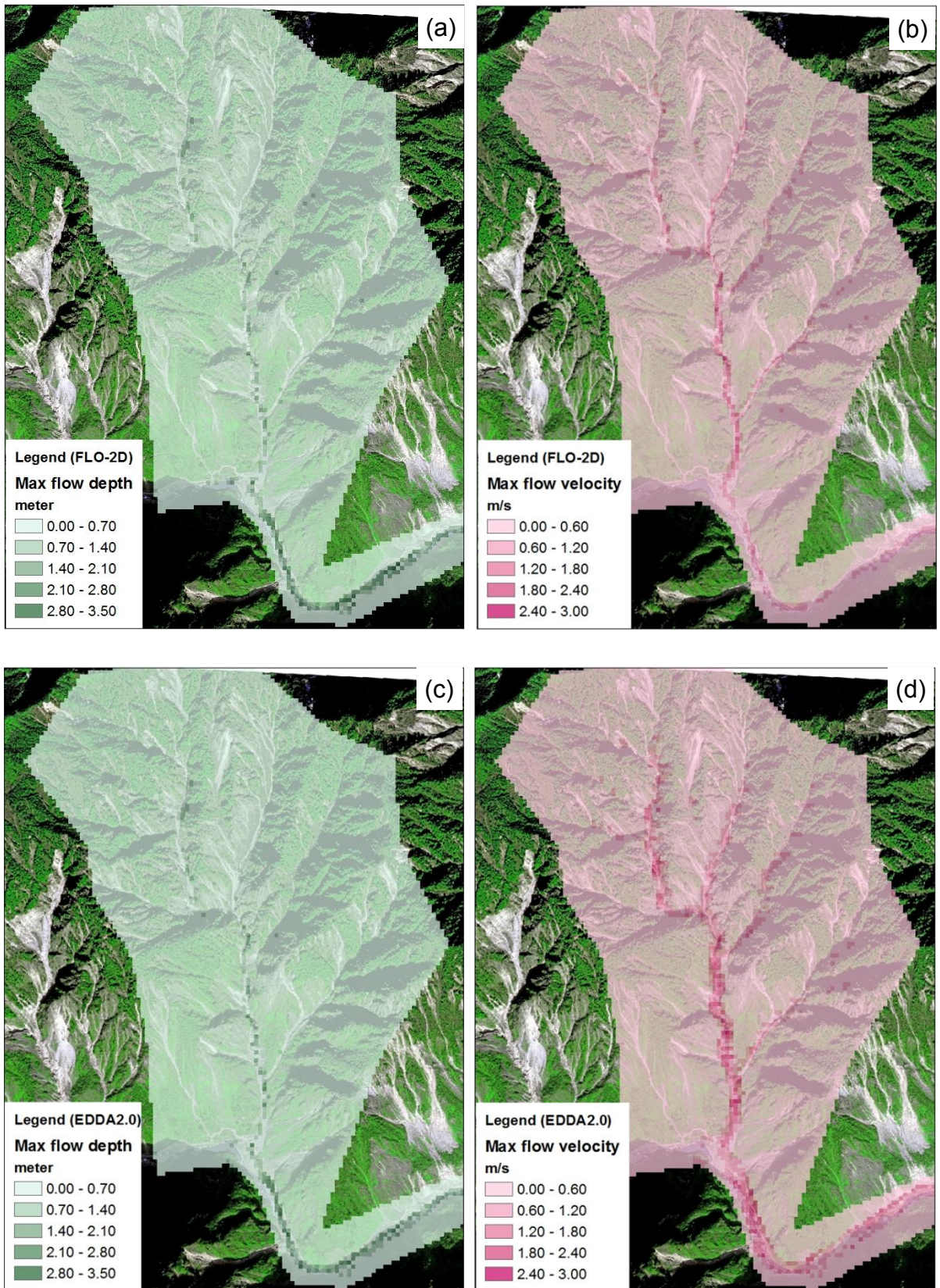
Figure 6. Comparison of the maximum surface runoff flow depths and flow velocities simulated using FLO-2D [(a) and (b)] and EDDA 2.0 [(c) and (d)].
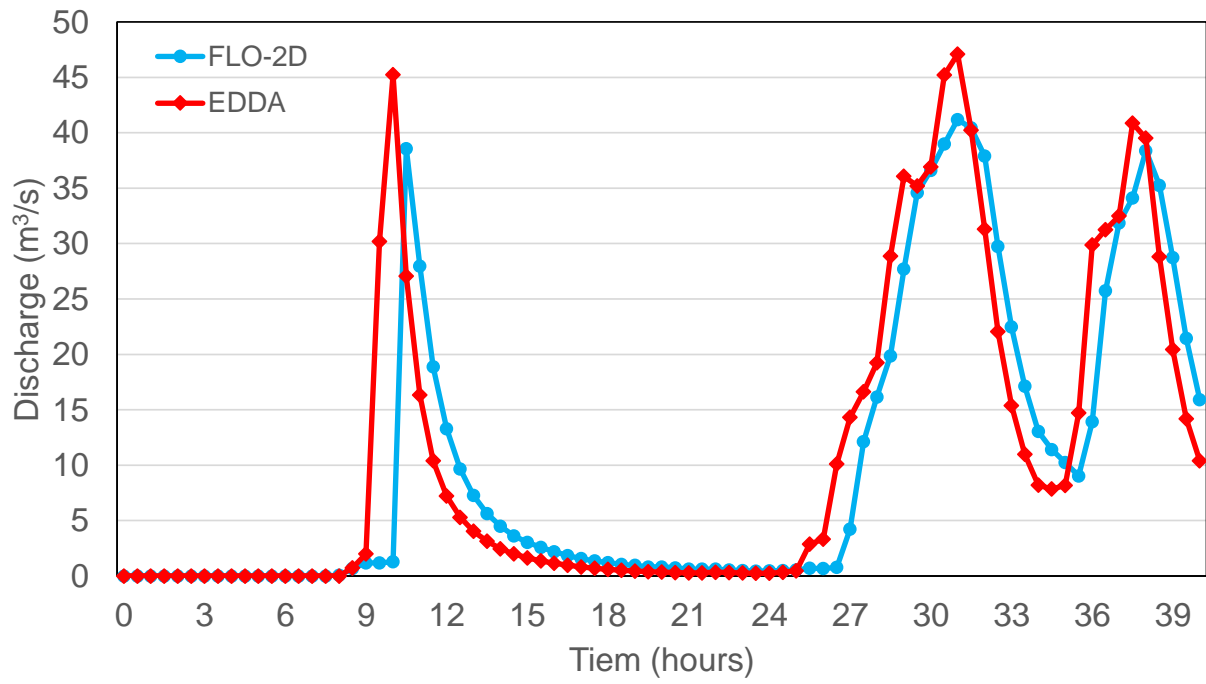
Figure 7. Comparison of the outflow hydrographs at the ravine mouth using FLO-2D and EDDA 2.0.
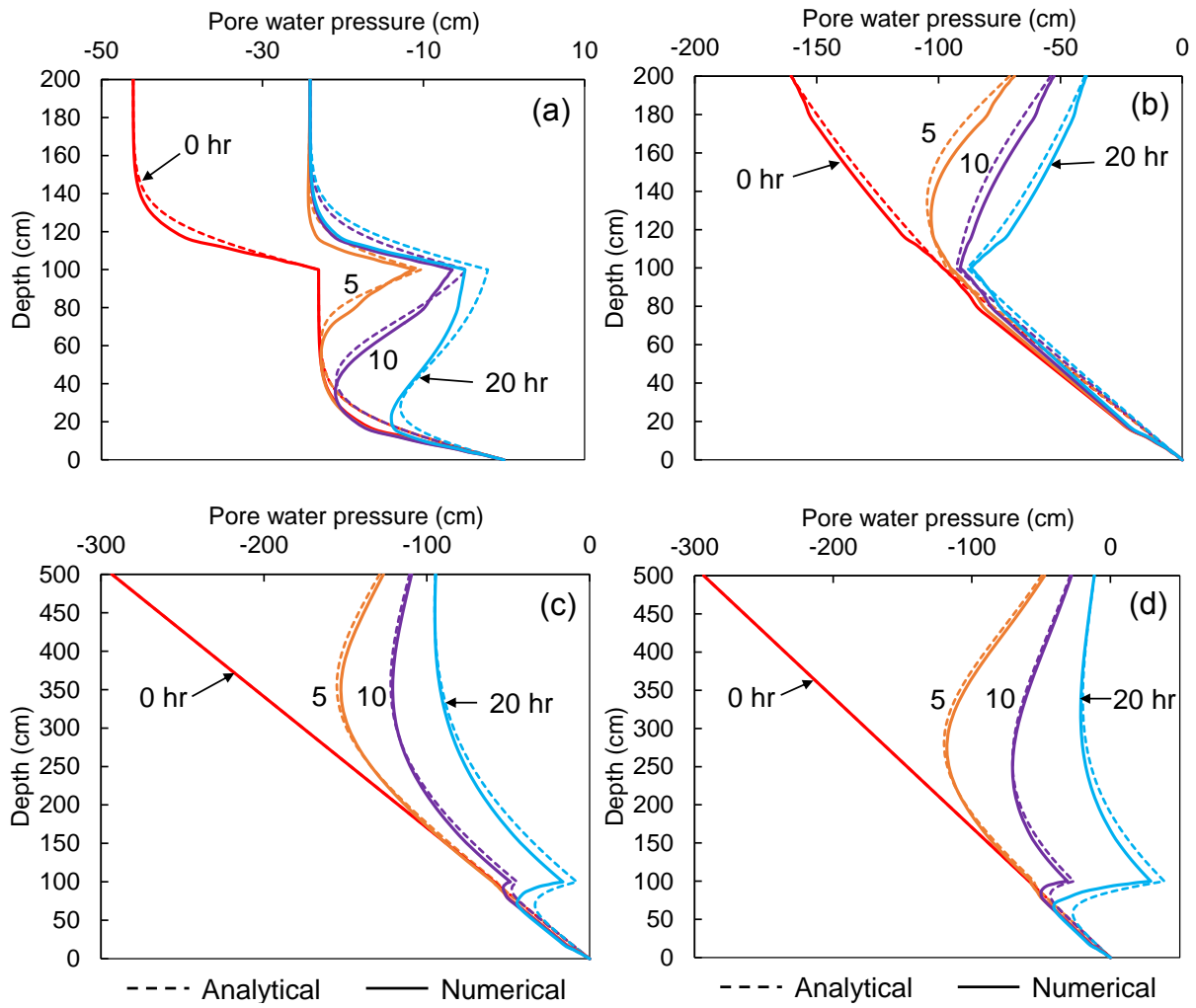
Figure 8. Pore water pressure profiles at various times: (a) Case 1; (b) Case 2; (c) Case 3; (d) Case 4.
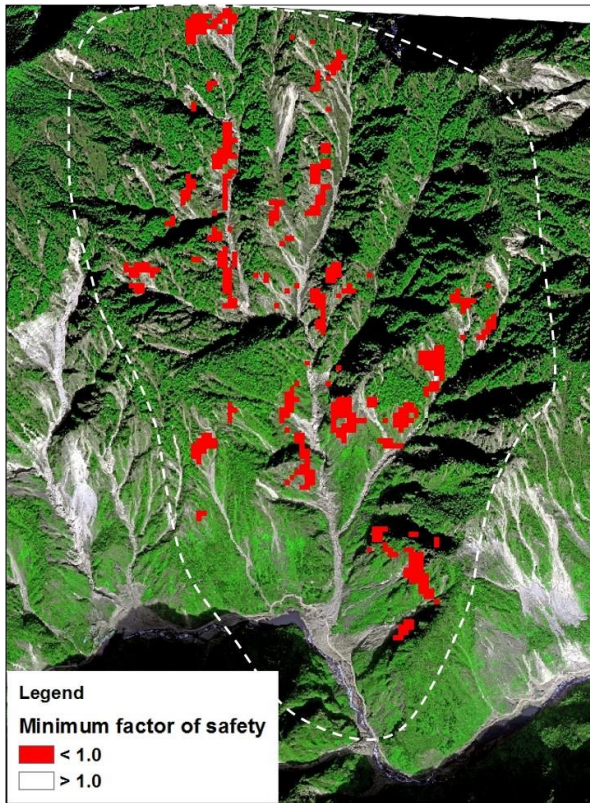
Figure 9. Computed unstable cells vs. landslide scars on the satellite image.
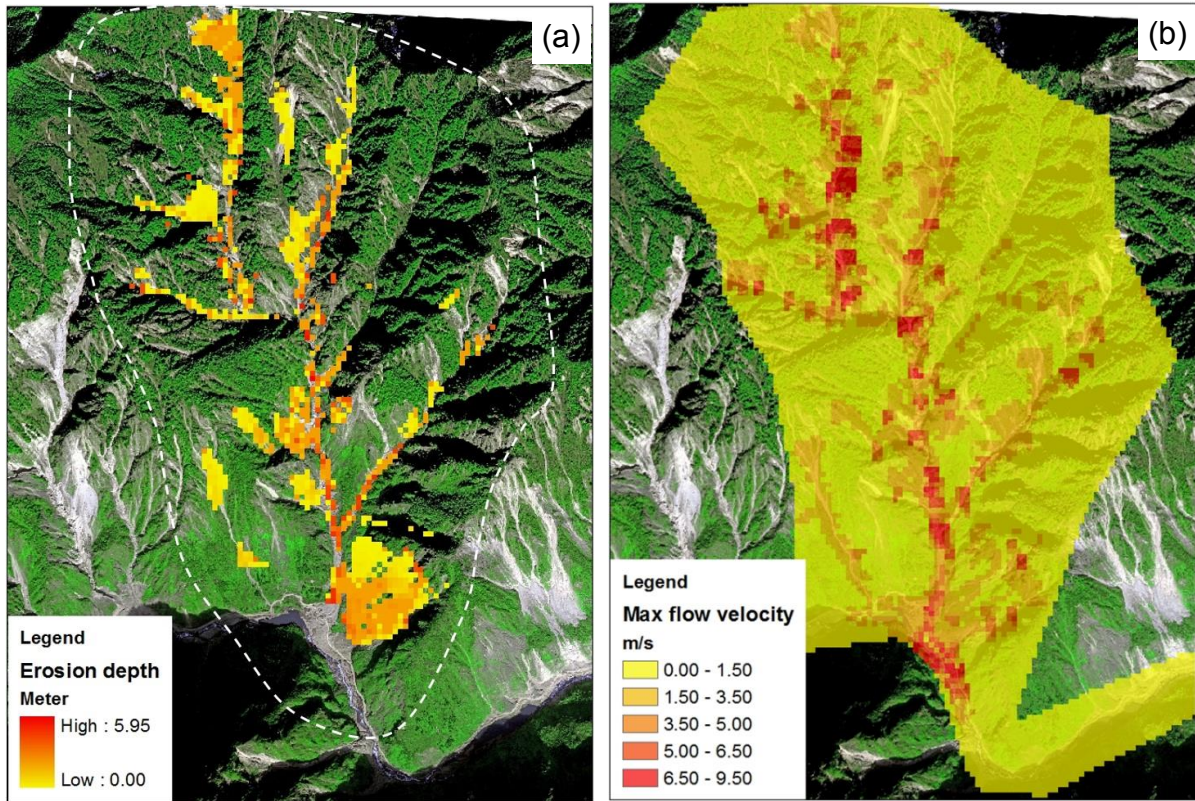
Figure 10. Simulation results of the Xiaojiagou debris flow: (a) final shape and depth of the erosion zone; (b) maximum flow velocity.
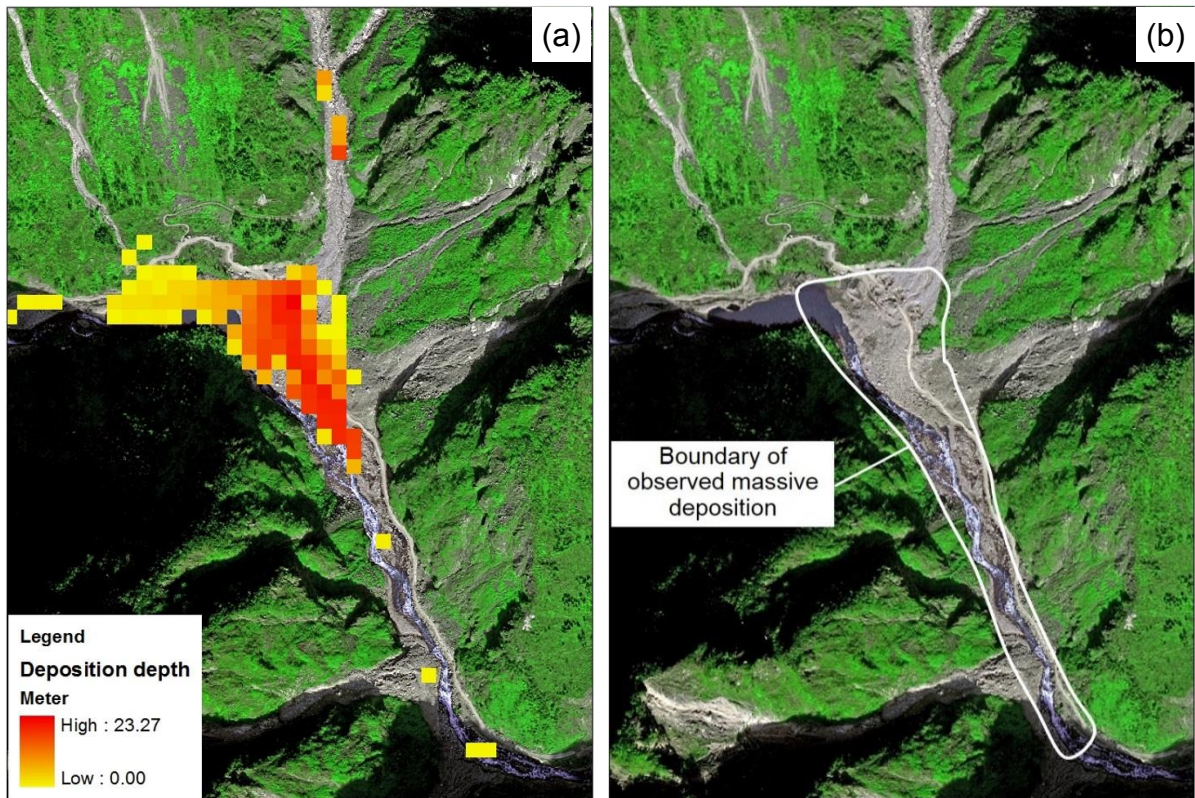
Figure 11. Comparison of the simulated and observed deposition zones: (a) simulation result; (b) enlarged view of the observed deposition area (Chen and Zhang, 2015).
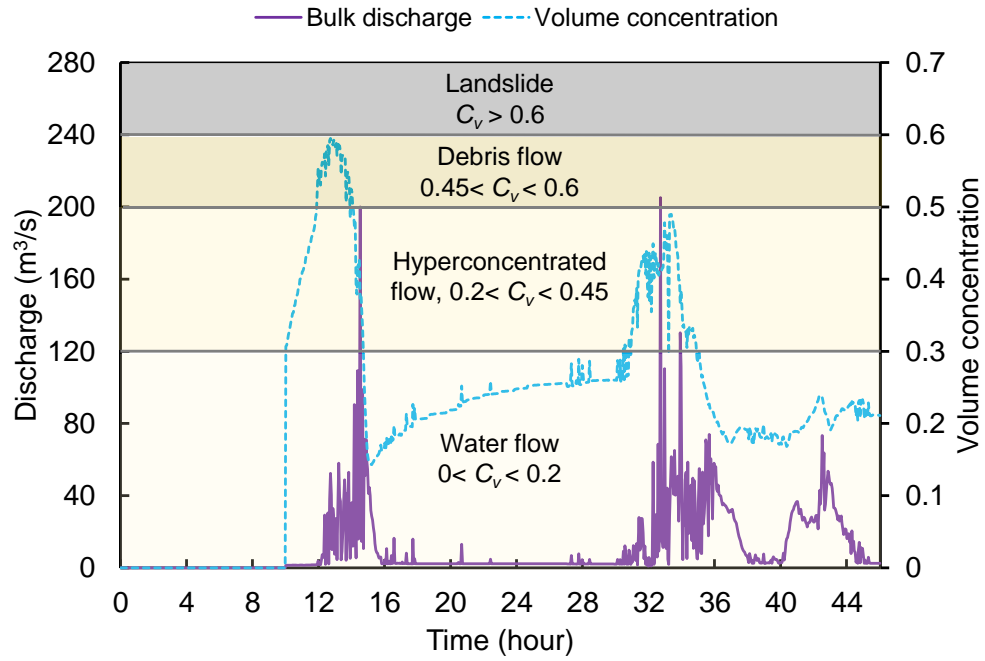
Figure 12. Outflow hydrograph and changes in C_v at the Xiaojiagou Ravine mouth during the simulation period.
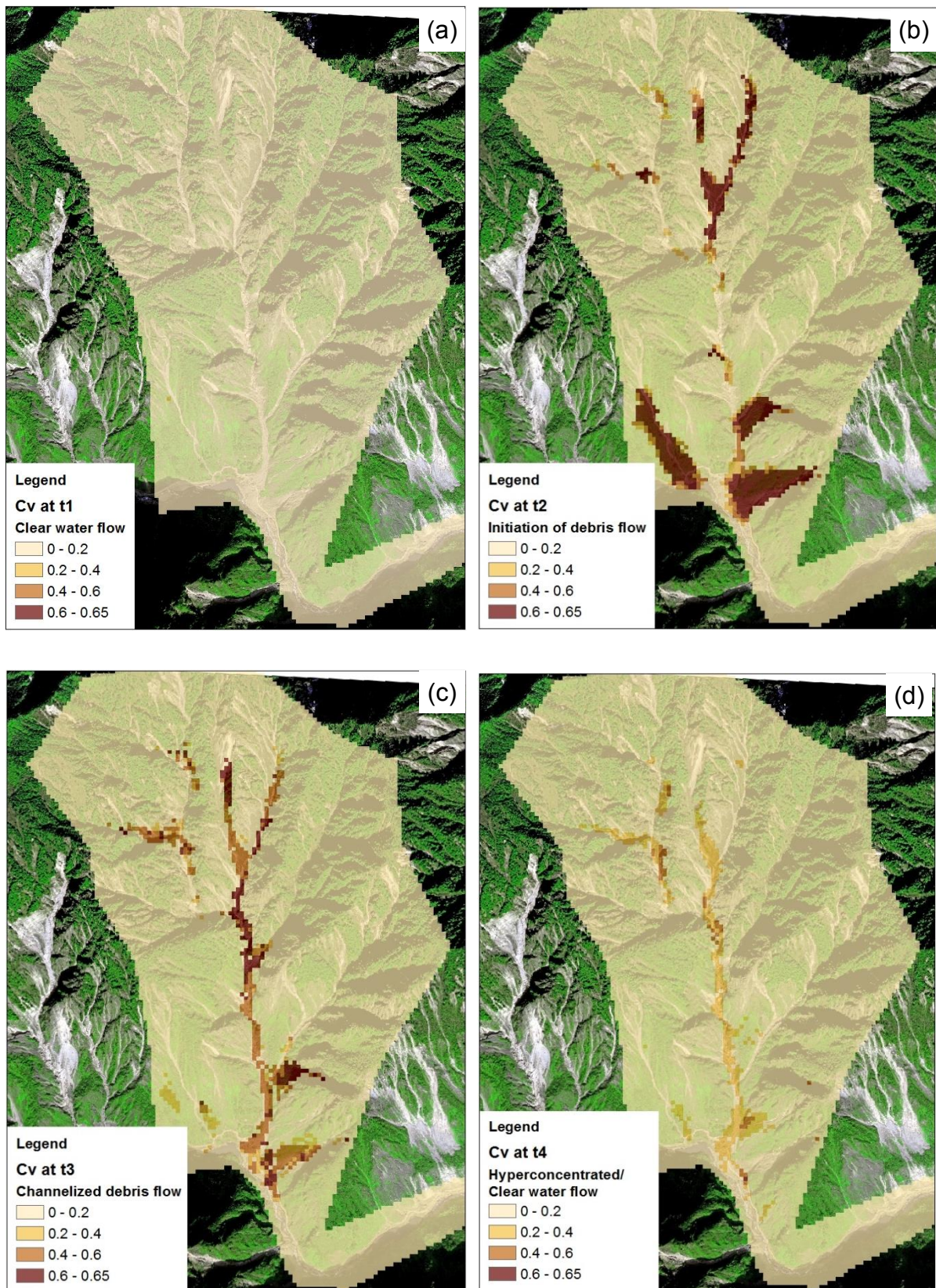
Figure 13. Distributions of C_v at different times of the storm event: (a) clear water flow; (b) initiation of debris flows; (c) channelized debris flows; (d) post hyperconcentrated/clear water flow.